CHEMISTRY OF MATERIALS
Article
Cite This: Chem. Mater. 2018, 30, 163−173
pubs.acs.org/cm

Probing Solid−Solid Interfacial Reactions in All-Solid-State Sodium-Ion Batteries with First-Principles Calculations

Hanmei Tang,[†] Zhi Deng,[†] Zhuonan Lin,[‡] Zhenbin Wang,[†] Iek-Heng Chu,[†] Chi Chen,[†] Zhuoying Zhu,[†] Chen Zheng,[†] and Shyue Ping Ong*,[†]

[†]Department of NanoEngineering, University of California, San Diego, 9500 Gilman Drive, Mail Code 0448, La Jolla, California 92093-0448, United States

[‡]Materials Science and Engineering Program, University of California, San Diego, 9500 Gilman Drive, Mail Code 0418, La Jolla, California 92093-0418, United States

Supporting Information

ABSTRACT: We present an exposition of first-principles approaches to elucidating interfacial reactions in all-solid-state sodium-ion batteries. We will demonstrate how thermodynamic approximations based on assumptions of fast alkali diffusion and multispecies equilibrium can be used to effectively screen combinations of Na-ion electrodes, solid electrolytes, and buffer oxides for electrochemical and chemical compatibility. We find that exchange reactions, especially between simple oxides and thiophosphate groups to form PO_4^{3-}, are the main cause of large driving forces for cathode/solid electrolyte interfacial reactions. A high reactivity with large volume changes is also predicted at the Na anode/solid electrolyte interface, while the $Na_2Ti_3O_7$ anode is predicted to be much more stable against a broad range of solid electrolytes. We identify several promising binary oxides, Sc_2O_3, SiO_2, TiO_2, ZrO_2, and HfO_2, that are similarly or more chemically compatible with most electrodes and solid electrolytes than the commonly used Al_2O_3 is. Finally, we show that *ab initio* molecular dynamics simulations of the $NaCoO_2/Na_3PS_4$ interface model predict that the formation of SO_4^{2-}-containing compounds and Na_3P is kinetically favored over the formation of PO_4^{3-}-containing compounds, in contrast to the predictions of the thermodynamic models. This work provides useful insights into materials selection strategies for enabling stable electrode/solid electrolyte interfaces, a critical bottleneck in designing all-solid-state sodium-ion batteries, and outlines several testable predictions for future experimental validation.

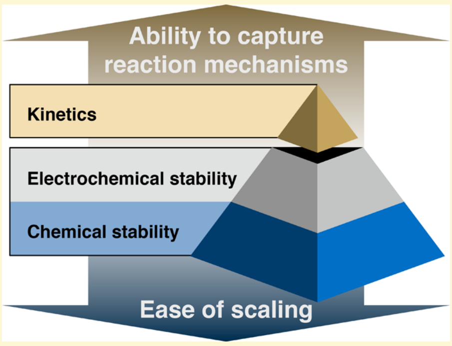

INTRODUCTION

All-solid-state rechargeable alkali-ion batteries (SSABs) have garnered significant interest in recent years.[1] With the replacement of flammable organic solvent electrolytes with nonflammable solid electrolytes, SSABs promise to be a safer energy storage architecture while, at the same time, potentially providing significant gains in system-level energy densities through device optimization (e.g., stacking) or enabling new chemistries (e.g., high-voltage cathodes and alkali metal anodes).[2,3]

Despite groundbreaking discoveries of novel solid electrolyte (SE) chemistries exhibiting superionic alkali conductivities,[4−9] a major challenge that remains is the unsatisfactory rate performance and cycling stability of SSABs due to the high resistance and poor stability of the electrode/SE interface. For example, though the $Li_{9.54}Si_{1.74}P_{1.44}S_{11.7}Cl_{0.3}$ based on the $Li_{10}GeP_2S_{12}$ (LGPS) structure first reported by Kato et al.[10] has one of the highest Li^+ conductivities (25 mS/cm), its extremely poor electrochemical stability and interfacial side reactions render it far less practical than $Li_{9.6}P_3S_{12}$, a material reported in the same work with a significantly lower conductivity (1.2 mS/cm) but much better interfacial stability. For Na-ion chemistry, most room-temperature solid-state Na batteries reported thus far suffer from limited capacity or significant capacity degradation during cycling.[9,11−16]

It is therefore not surprising that researchers have escalated their efforts to understand and address these interfacial issues in SSABs. On the experimental front, X-ray photoelectron spectroscopy (XPS) has emerged as a common approach for probing and identifying the species present at the buried electrode/SE interface.[17−19] The application of buffer layers such as Al_2O_3 has been demonstrated to be an effective approach for improving the wetting of the electrode/SE interface (especially for Li metal anodes),[20] as well as a protective barrier to electrode/SE reactions (especially for sulfide SEs).[21−23] Also, first-principles calculations have emerged as an important complementary tool for precisely probing interfacial reactions[24,25] and the electrochemical stability of SEs. Ong, Mo, and Ceder[26,27] first developed the first-principles Li grand potential approximation to predict SE phase equilibria at the high and low voltage limits in the LGPS family of SEs. This approximation has been shown to be

Received: September 27, 2017
Revised: December 12, 2017
Published: December 12, 2017

DOI: 10.1021/acs.chemmater.7b04096
Chem. Mater. 2018, 30, 163−173

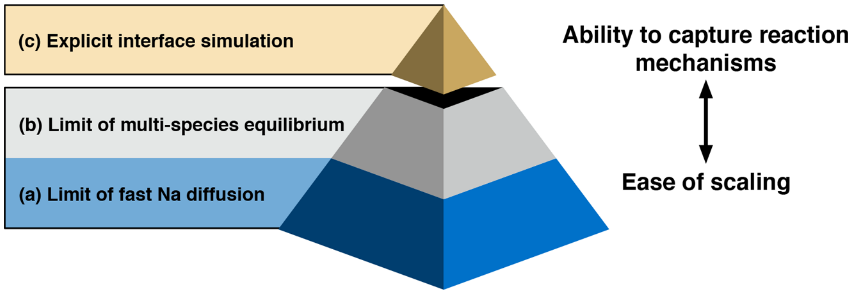

Figure 1. Hierarchy of models for solid/solid interface reactions. (a) Fast diffusion of alkali ion (grand potential phase diagram). (b) Multispecies equilibrium, e.g., slow diffusion or an extremely long time scale (reaction prediction using a pseudobinary phase diagram). (c) *Ab initio* molecular dynamics (AIMD), accounting for different multispecies mobilities and interactions at finite temperatures. The thermodynamic models at the bottom of the pyramid are computationally less costly but make various assumptions about species mobilities. The AIMD approach captures kinetics at finite temperatures, but the high computational cost limits such simulations to small model systems and short simulation time scales.

remarkably effective, as evidenced by subsequent experimental confirmation of the predicted reaction phases via XPS measurements.[17] Later, these approaches were further extended to extensive studies of most well-known Li and Na SEs.[14,28−32] More recently, Tian et al. reported a combined experimental and theoretical study of the compatibility of the Na_3PS_4 and Na_3PSe_4 SEs with layered transition metal oxide ($NaTmO_2$, where Tm = Cr, Mn, Fe, Co, or Ni) cathodes.[19]

In this work, we will attempt to address two crucial gaps in previous works. First, previous works have primarily focused on thermodynamic approximations to interfacial phase equilibria; the previous studies accounted for kinetic effects to an only limited extent,[19] if at all. Second, a comprehensive assessment of Na-ion electrode/SE interactions has not been performed, and in general, there is a lack of guidance on effective materials selection strategies for cathode/SE, anode/SE, and buffer layers for all-solid-state Na-ion batteries (SSNaBs). In the subsequent sections, we will first outline the various approximation methodologies for predicting interfacial phase equilibria, including explicit kinetic interface model analysis using *ab initio* molecular dynamics (AIMD) combined with radial distribution function analysis. This is followed by a comprehensive study of the reactions among the common cathode, anode, and SE chemistries currently under consideration for SSNaBs, along with recommended materials selection strategies. Furthermore, we will also attempt to provide a rough estimate of the chemomechanical effect of these reactions, a factor not considered in previous works.

■ MODELS FOR SOLID−SOLID INTERFACES

Here, we will outline the general principles behind the various first-principles approaches for predicting solid/solid interface equilibria and reactivity. Figure 1 provides an overview of the three models that will be discussed in this section, arranged in order of complexity. The bottom two models are based on thermodynamic approximations, and they have been used in previous works on Li SEs;[26−32] the model on the top of the pyramid is an explicit interfacial model simulated at finite temperatures. We will discuss these models in the context of SSNaBs, though the models can be similarly applied to SSLiBs.

Approach 1: Fast Diffusion of an Alkali Ion. Under the assumption that Na is the main mobile species, the SE material can be treated as an open system to Na described by chemical potential μ_{Na}. The SE is subjected to a maximum range of electrochemical potentials when the battery is fully charged, where the desodiated cathode is effectively a Na sink at a low μ_{Na} and the sodiated anode is effectively a Na source at a high μ_{Na}. The electrochemical window of a SE is essentially the μ_{Na} or voltage range in which the composition of SE is stable against either Na extraction or insertion, which can be estimated using the density functional theory (DFT) grand potential phase diagram at various μ_{Na} values.[33] The Na grand potential is given by

$$\phi(c, \mu_{Na}) = E(c) - \mu_{Na}N(c) \qquad (1)$$

where $E(c)$ is the total energy from DFT calculations and $N(c)$ is the number of Na atoms of that particular phase with composition c. μ_{Na} is related to voltage V with respect to the Na metal anode by

$$V = -\frac{\mu_{Na} - \mu_{Na}^{0}}{e} \qquad (2)$$

where μ_{Na}^{0} is the Na chemical potential of Na metal and e is the electron charge.

In essence, one can view this as an estimate of the electrochemical (grand canonical) stability of the SE with respect to voltage. Henceforth, we will simply refer to this estimate as the electrochemical stability for the sake of brevity.

Approach 2: Multispecies Equilibrium. In this approach, the assumption is that the two materials at a heterogeneous interface react to form the most favorable products under full thermodynamic equilibrium.[29−32] The most favorable reaction is determined by constructing the pseudobinary phase diagram between the two materials, a and b (e.g., between the $NaCoO_2$ cathode and the Na_3PS_4 SE), and finding the reaction ratio resulting in the most negative reaction energy:

$$\Delta E(c_a, c_b) = \min_{x\in[0,1]} \frac{1}{N}\{E_{eq}[xc_a + (1-x)c_b] - xE[c_a] - (1-x)E[c_b]\} \qquad (3)$$

where c_a and c_b are the compositions of phases a and b, respectively, x is the ratio of c_a, $E[c_a]$ and $E[c_b]$ are the DFT total energies of phases a and b, respectively, $E_{eq}(c)$ is the energy of phase equilibria at composition c, and N is a normalization factor, which is equal to the total number of atoms involved in the reaction. $\Delta E(c_a,c_b)$ may then be regarded as an estimate of the chemical (equilibrium) stability of the two materials with each other. Henceforth, we will simply refer to this estimate as the chemical stability for the sake of brevity. The more negative the $\Delta E(c_a,c_b)$, the greater the thermodynamic driving force for the two materials to react at a heterogeneous interface.

In addition, we can also estimate volume change ΔV as a result of the reaction at a heterogeneous interface by comparing the volumes of products of the reaction to that of the reactants in the reaction. The final DFT relaxed volumes of each reactant/product pair are used in this estimate. A negative ΔV means that the volume of the products is smaller than that of the reactants, which may cause the formation of voids and a loss of contact at the interface. On the other hand, a positive ΔV means that the volume of the products is larger than that of the reactants, which may cause the buildup of stresses and cracks at the interface.

Approach 3: Explicit Interface Simulation. In the third approach, finite-temperature *ab initio* molecular dynamics (AIMD) simulations are performed on explicit models constructed for solid/solid interfaces in a SSNaB, as shown in Figure 2.

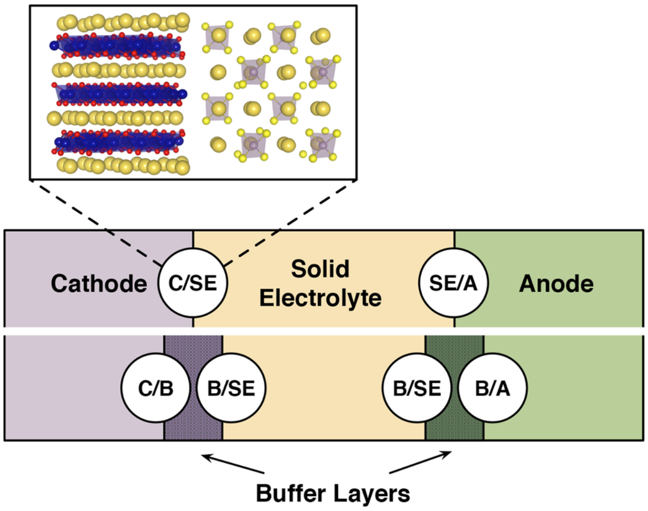

Figure 2. Schematic diagram of interfaces in SSNaBs without buffer layers (top) and with buffer layers (bottom). Letters in the figure denote the cathode (C), the solid electrolyte (SE), the anode (A), and the buffer layer (B). The atomic structures of interfaces are provided in Table S4 and Figure S3).

Interface Construction. The interface models were constructed using slabs of electrodes, buffer layers, or SE material. The orientation of the cathode slab was chosen such that it is a low-energy surface appearing in the calculated Wulff shape[34] that also presents facile channels for Na diffusion. A similar criterion was used by Haruyama et al.[35] The spacing between two materials was initially set at 2.5 Å. To achieve a good compromise between the number of atoms in the model and the misfit strain at the interface, we used the algorithm proposed by Stradi et al.[36] to identify the optimal supercell combination based on the following criteria:

Lattice misfit parameter $m < 6\%$.

$$m = \frac{|p_i - p_s|}{p_i} \times 100\% \tag{4}$$

where p_i and p_s are perimeters of the unit cell $a-b$ plane of the interface and the slab, respectively.

Mean absolute strain $\bar{\varepsilon} < 10\%$.

$$\bar{\varepsilon} = \frac{|\varepsilon_{xx}| + |\varepsilon_{xy}| + |\varepsilon_{yy}|}{3} \tag{5}$$

where ε_{xx}, ε_{xy}, and ε_{yy} are components of plane strain caused by matching one slab with another.

Changes in bonding were tracked over the course of AIMD simulations for at least 30 ps (with transition metal) and 160 ps (without transition metal) by comparing the radial distribution functions (RDFs) of various species at the interface with those of all known reference crystalline compounds within the chemical system of interest. For instance, in the case of the Na_3PS_4/Na interface, the interfacial RDFs are compared with those of all known compounds in the Na−P−S chemical space, i.e., all Na, P, S, Na_xP_y, Na_xS_y, P_xS_y, and $Na_xP_yS_z$ phases in the Materials Project (MP) database[37,38] with an energy above hull (E_{hull}) of <20 meV/atom. E_{hull} is a measure of the stability of a reference material, and here, we limit the reference collection to relatively stable phases, as shown in Table S5. We will discuss our systematic process of elimination to identify matching reference compounds, e.g., by noting the absence or presence of well-defined bond lengths such as those for PO_4^{3-}, SO_4^{3-}, and PS_4^{3-} tetrahedra, in the Results. It should also be noted that we did not explicitly set any interfacial reactions to be driven by the inherent concentration/chemical potential gradients across the interface, and the voltage is not explicitly set in the AIMD simulations.

Materials Selection. The relatively low computational cost of thermodynamic approaches 1 and 2 described above permits a high-throughput analysis of a large number of material combinations forming the interface, especially if precomputed energies and volumes from the MP database are used where available. As such, we have performed a comprehensive analysis covering most well-known SE, cathode, and anode materials across a broad range of chemistries currently of interest in the Na-ion battery community, as shown in Table 1.

Table 1. Cathode, Solid Electrolyte, Anode, and Buffer Layer Materials Studied Using Thermodynamic Approaches 1 and 2

category	materials
solid electrolytes	NASICON $Na_3Zr_2Si_2PO_{12}$,[4,55] Na_3PS_4[9,12]
	Na_3AsS_4,[15] Na_3SbS_4,[13,46,56] Na_3PSe_4[57,58]
cathodes	layered $NaMO_2$ (M = Cr, Mn, Fe, Co, or Ni)[59−62]
	layered TiS_2[63]
	$NaFePO_4$,[64] Na_2FePO_4F[65]
	$Na_3V_2(PO_4)_3$,[66] $Na_3V_2(PO_4)_2F_3$,[67] $Na_2Fe_2(SO_4)_3$[68]
anodes	Na metal, $Na_2Ti_3O_7$[69]
buffer layers	ZnO, CdO
	Al_2O_3, Sc_2O_3, Y_2O_3, La_2O_3
	SiO_2, TiO_2, ZrO_2, HfO_2
	Nb_2O_5, Ta_2O_5

More details regarding selected structures for thermodynamic interfacial reactivity assessments can be found in Table S1.

Given the high computational expense of AIMD simulations of interfacial systems, approach 3 was applied for only one model battery system, layered O3-$NaCoO_2$ cathode, Na_3PS_4 SE, and Na metal anode, with Al_2O_3 as the model buffer layer. For the $NaCoO_2$ cathode, both the half-discharged and fully discharged cathode materials were modeled to assess the effect of the state of charge on interfacial reactivity. All structures used to construct interfaces are relaxed structures from the MP database, and details are listed in Table 2.

Table 2. Selected Structures for Interface Constructions

	cathode	solid electrolyte	anode	buffer layer
formula	$NaCoO_2$	Na_3PS_4	Na	Al_2O_3
MP id	mp-18921	mp-985584	mp-127	mp-1143
space group	$R\bar{3}m$	$I\bar{4}3m$	$Im\bar{3}m$	$R\bar{3}c$
slab orientation	$(10\bar{1}0)$	(001)	(001)	(0001)

DFT Calculation Parameters. All calculations were performed using the Vienna *Ab initio* Simulation Package (VASP)[39] within the projector-augmented wave approach[40] using the Perdew−Burke−Ernzerhof generalized-gradient approximation (GGA) functional.[41]

For total energy calculations, a mixing scheme combining GGA calculations with or without Hubbard (+U) correction was applied to treat electron insulators and conductors properly.[42] All parameters, such as a plane wave energy cutoff of 520 eV and a k-point density of at least 1000/(number of atoms), were chosen in a manner consistent with those used in MP as implemented in the Python Materials Genomics (pymatgen)[43] package. All calculations were spin-polarized starting from a high-spin ferromagnetic configuration, except for Co, which is initialized with low spin.

For AIMD simulations, non-spin-polarized calculations were performed using a minimal Γ-point k-point grid and a time step of 2 fs. The use of non-spin-polarized calculations is a necessary approximation to ensure the AIMD simulations can be performed at a reasonable cost, and we do not expect the key results (reaction mechanisms and products at the interface) to be significantly affected by this approximation. Simulations in the NpT ensemble at 300 K were first performed until the volume of the cell converged to within 2%. This step is necessary to minimize the interfacial stress caused by the lattice misfit and typically occurs within 4 ps of simulation time (Figure S9). The pressure of NpT simulations was kept at 1 atm with the Langevin thermostat,[44] and a larger plane wave energy cutoff of 400 eV (without oxygen) or 600 eV (with oxygen) was used to avoid the undesired Pulay stress error. This is followed by NVT simulations at 300 K using a smaller energy cutoff of 280 eV (without oxygen) or 400 eV (with oxygen) and the Nose-Hoover thermostat. All calculations were performed using automated in-house AIMD workflow software.[45]

■ RESULTS

Electrochemical (grand canonical) Stability. Figure 3 shows the predicted electrochemical window of various SEs calculated using the grand potential phase diagram approach. We find that none of the commonly studied Na SEs are stable against Na uptake at a voltage close to that of Na metal. Generally, the NASICON $Na_3Zr_2Si_2PO_{12}$ oxide SE has better cathodic and anodic stability compared to those of sulfide SEs, which in turn have better cathodic and anodic stability compared to those of the selenide (Na_3PSe_4).

Figure 3 also shows the predicted phase equilibria and Na uptake versus voltage for the Na_3PS_4 SE. The predicted phase equilibria and Na uptake profile for the other SEs are available in Table S2 and Figure S1. The predicted products at the Na metal anode voltage are Na_3P and Na_2S, in good agreement with XPS measurements of Na_3PS_4 after Na metal deposition.[18] We also note that Na_3AsS_4 and Na_3SbS_4 show electrochemical windows that are significantly narrower than that of Na_3PS_4. This is due to the fact that As and Sb are redox-active elements. Interestingly and somewhat counterintuitively, both the immediate cathodic and anodic decomposition of Na_3AsS_4 and Na_3SbS_4 occur with the reduction of As/Sb from the 5+ to the 3+ oxidation state, with the formation of Na_2S with Na uptake (reduction at low voltages) and S with Na extraction (oxidation at high voltages). Details of the reaction products are provided in Table S2.

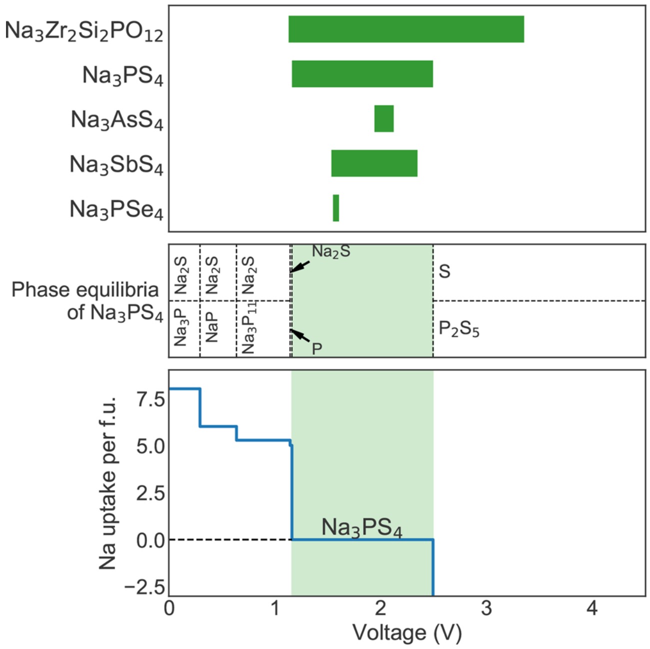

Figure 3. Electrochemical stability of studied solid electrolytes (top). Predicted phase equilibria over different voltage (μ_{Na}) ranges for one example solid electrolyte, Na_3PS_4 (middle). Na uptake per formula unit of Na_3PS_4 vs voltage (bottom).

It should be noted that the predicted products for Na_3PS_4 and Na_3PSe_4 differ slightly from those in earlier work by Tian et al.[19] because this study uses only data available in the Materials Project without including predicted phases. Nevertheless, the main qualitative conclusion is the same, which is that both Na_3PS_4 and Na_3PSe_4 have limited electrochemical windows, which are much narrower than those from cyclic voltammetry (CV) measurements.[12,46]

Chemical (equilibrium) Stability. ***Electrode/SE Interfacial Stability.*** Figure 4 shows the calculated reaction energies (left) and volume changes (right) between various discharged electrode/SE pairs using approach 2. The corresponding reaction products are listed in Table S3. We may make the following key observations.

(1) Highly unstable cathode/SE combinations arise when a non-polyanion cathode (such as the layered $NaMO_2$ oxides) is paired with Na_3PS_4 or Na_3PSe_4 because of the displacement reaction of the S^{2-} or Se^{2-} by O^{2-} to form the highly stable PO_4 compounds, e.g., $NaCrO_2 + Na_3PS(Se)_4 \rightarrow Na_3PO_4 + NaCrS(Se)_2$. This observation is consistent with those made previously by Richards et al.[30] and Tian et al.[19] The volume changes depend on the transition metal species, with $NaCoO_2$, $NaNiO_2$, and $NaMnO_2$ exhibiting relatively large positive volume changes.

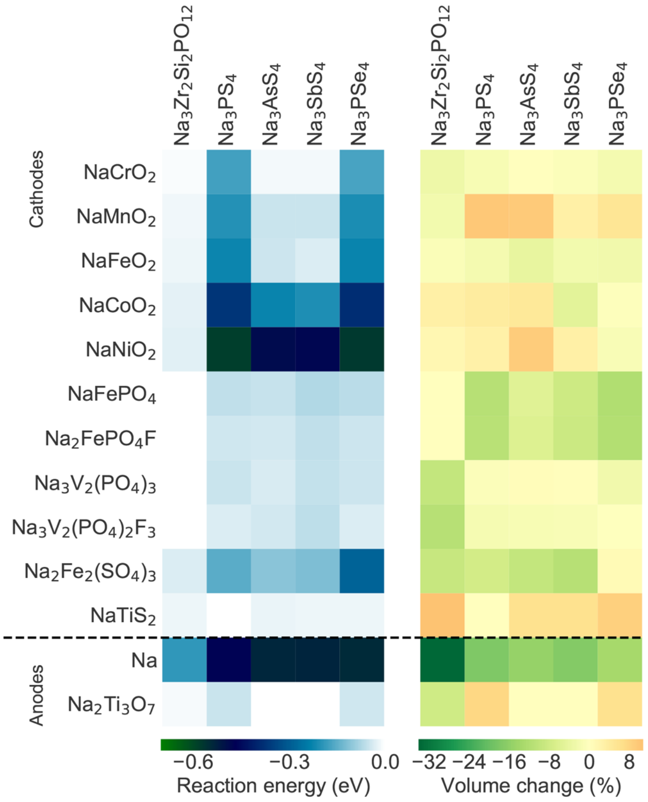

Figure 4. Reaction energies (left) and volume changes (right) for electrode/SE pairs. The reactions are calculated for the discharged cathode.

(2) Substitution of P with As and Sb tends to improve the chemical stability of the layered $NaMO_2$/SE interface. Though the DFT phase diagrams still predict the occurrence of exchange reactions, these tend to be incomplete in the case of As and Sb; i.e., not all As or Sb is consumed during the formation of As_xO_y or Sb_xO_y polyanions, respectively, which may account for the reaction energy being lower than that of P.

(3) The PO_4-containing polyanion cathodes [$NaFePO_4$, $NaFePO_4F$, $Na_3V_2(PO_4)_3$, and $Na_3V_2(PO_4)_2F_3$] show significantly better chemical stability with all sulfide and selenide SEs. However, the two Fe-containing cathodes, $NaFePO_4$ and $NaFePO_4F$, are predicted to exhibit relatively larger negative volume changes upon reactions with sulfide and selenide SEs, while the two V-containing cathodes, $Na_3V_2(PO_4)_3$ and $Na_3V_2(PO_4)_2F_3$, show comparatively smaller volume changes ($|\Delta V| < 2.5\%$). The main reason is the reaction products for the Fe-based cathodes lack low-density chalcogenides (e.g., Na_2S and VS_2). The SO_4-containing $Na_2Fe_2(SO_4)_3$ has a chemical stability between those of the PO_4-containing and non-polyanion oxide cathodes.

(4) Unsurprisingly, the NASICON $Na_3Zr_2Si_2PO_{12}$ shows the best chemical compatibility with all oxide cathodes among the SEs.

(5) $NaTiS_2$ shows good compatibility with all sulfide and selenide SEs. Somewhat surprisingly, the chemical stability of the NASICON/$NaTiS_2$ interface is predicted to be worse than that of the NASICON/PO_4-containing cathode interface. A NASICON/PO_4-containing cathode interface has either no reaction (e.g., $NaFePO_4$ and Na_2FePO_4F) or a nonredox reaction with a negligible driving force [e.g., $Na_3V_2(PO_4)_3$ and $Na_3V_2(PO_4)_2F_3$], while the NASICON/$NaTiS_2$ interface undergoes a redox reaction with a larger driving force.

(6) Finally, a highly reactive Na metal anode is predicted to be chemically unstable with all SEs, with large negative volume changes. $Na_2Ti_3O_7$ shows much better chemical−mechanical compatibility, with especially low reaction energies and small volume changes with the Na_3AsS_4 and Na_3SbS_4 SEs.

We have performed a similar analysis using a few selected cathodes in the charged state (as opposed to discharged). The results are available in Figure S2 and Table S3). Generally, charged cathodes are more oxidizing than discharged cathodes, resulting in more negative reaction energies and larger volume changes. Nevertheless, we find that the overall trends in chemical stability across cathode/SE chemistry pairs remain fairly consistent with that of the discharged cathodes.

Evaluation of Potential Buffer Layer Materials. Binary oxides are commonly used as buffer layer materials to protect the electrode/electrolyte interface in alkali-ion batteries.[47,48] A good buffer layer material should exhibit limited reactivity with both materials at the heterogeneous interface. Figure 5 shows the calculated reaction energies of potential buffer layer materials and active materials in SSNaBs. We find that Al_2O_3, a commonly used buffer layer material,[49] shows extremely low reactivity with most SEs and cathodes and slight reactivity with Na metal. Interestingly, HfO_2 is predicted to be another particularly promising buffer layer material, showing even lower reactivity across nearly all SEs and electrodes compared to that of Al_2O_3. Indeed, there have been a few attempts to use

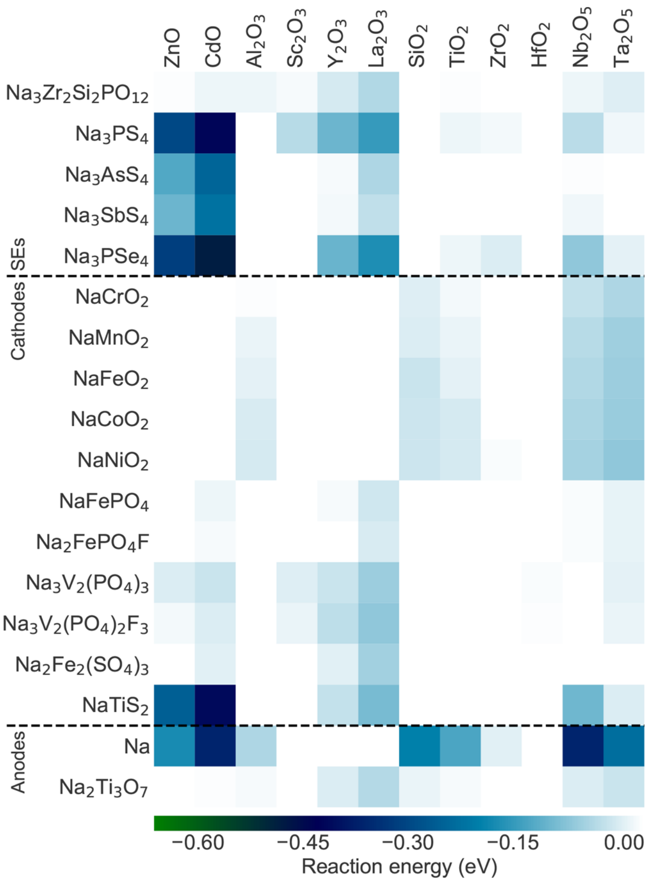

Figure 5. Reaction energies for potential buffer layer materials (binary oxides) and various active materials in SSNaBs.

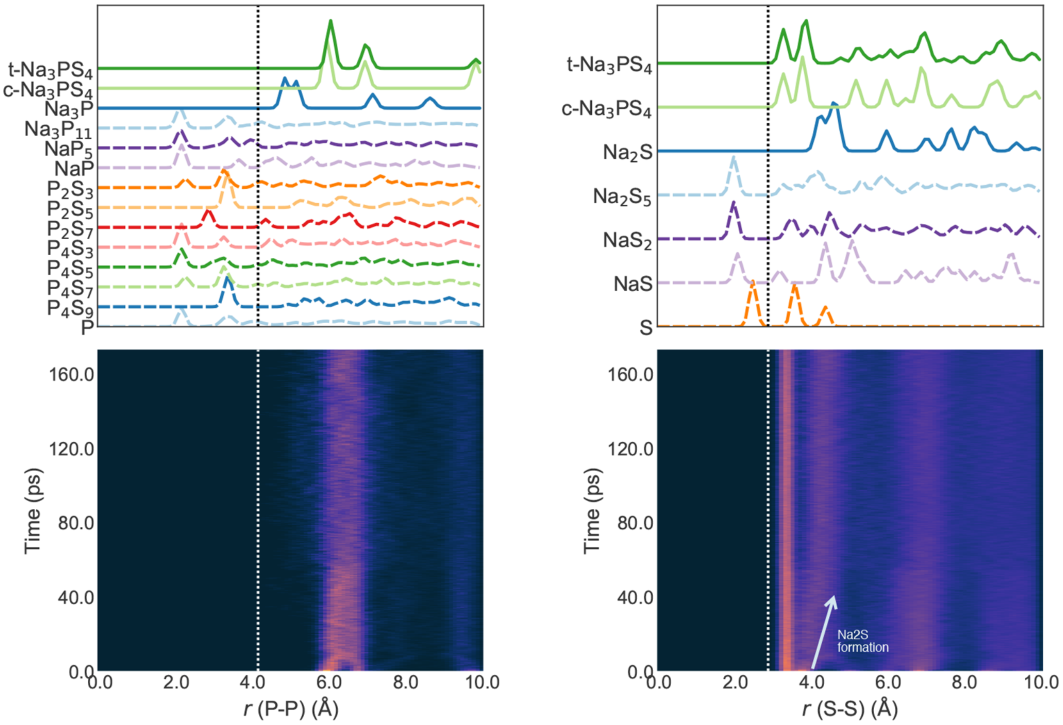

(a) P-P pair (b) S-S pair

Figure 6. Evolution of the (a) P−P and (b) S−S RDFs of the Na_3PS_4/Na interface with respect to AIMD simulation time plotted as a heat map, with a higher brightness indicating a higher value of $g(r)$. Dashed lines are used to indicate the RDF of phases that are eliminated because of the absence of certain peaks during the AIMD simulations. White arrows and text indicate the formation of interfacial reaction phases. The RDFs of reference materials are provided above the heat map. Note that t-Na_3PS_4 and c-Na_3PS_4 refer to the tetragonal and cubic phases, respectively.

HfO_2 as a protective material for anodes in alkali-ion batteries.[50,51] ZrO_2 is another promising candidate, as well, though it is predicted to have a somewhat higher reactivity with Na_3PSe_4. For the interface between polyanionic cathodes and SEs, SiO_2 is another inexpensive and stable option.

For the Na metal anode/SE interface, only HfO_2, Sc_2O_3, and ZrO_2 are predicted to have low reactivity with Na metal while maintaining low reactivity with the sulfide and selenide SEs.

AIMD Simulations of Explicit Interfacial Models. Because of the computational expense, AIMD simulations were performed on explicit interfacial models for one model system only, layered O3-$NaCoO_2$ cathode, Na_3PS_4 (cubic) SE, and Na metal anode, with or without Al_2O_3 as a buffer layer. For the $NaCoO_2$ cathode, both charged $Na_{0.5}CoO_2$ and fully discharged $NaCoO_2$ cathode materials were modeled to assess the effect of the state of charge on interfacial reactivity. It should be noted that layered oxides such as $NaCoO_2$ are typically charged only to half-theoretical capacity during operation to avoid the collapse of the layered structure; hence, we have used $Na_{0.5}CoO_2$ as the model for the charged cathode. A total of five interfacial models were studied (see Figure 2). We will outline the RDF analysis approach in greater detail using the comparatively simpler Na_3PS_4/Na interfacial system to illustrate the key principles, while only key results will be discussed for the other interfacial systems.

Na_3PS_4/Na (SE/anode) Interface. Figure 6 shows the evolution of the Na_3PS_4/Na interface model with respect to the simulation time. From Figure 6a, we may observe that there is a negligible density of <4.2 Å P−P bonds throughout the entire simulation, which eliminates P, P_xS_y, NaP, NaP_5, and Na_3P_{11} as potential phases that are present. From Figure 6b, we similarly observe that there is a negligible density of <2.9 Å S−S bonds, which further eliminates S, NaS_2, and Na_2S_5 as potential phases present at the interface. Through this process of elimination, we conclude that the potential phases present at the interface are Na_3PS_4, Na_3P, and Na_2S. We note that the RDFs in panels a and b of Figure 6 show no peaks corresponding to Na_3P [min r(P−P) ∼ 5.0 Å] and Na_2S [min r(S−S) ∼ 4.6 Å], respectively, at the start of the simulation ($t = 0$), but these peaks become progressively stronger over the course of the simulation. We may therefore conclude that the dominant reaction products at the Na_3PS_4/Na interface are Na_2S and Na_3P, which is consistent with the predicted interfacial reaction determined by thermodynamic approaches and previous experimental studies.[18]

$NaCoO_2$/Na_3PS_4 (cathode/SE) Interface. Figure 7 shows comparisons between the evolution of interface models with the discharged $NaCoO_2$ and charged $Na_{0.5}CoO_2$ cathode with respect to the simulation time. Unsurprisingly, we observe that the discharged cathode is much less reactive with the Na_3PS_4 SE than the more oxidizing charged cathode is. For instance, strong Na−Na peaks corresponding to $NaCoO_2$ persist throughout the entire length of the simulation (Figure 7a). We will henceforth focus our discussion on the charged $Na_{0.5}CoO_2$/Na_3PS_4 interface.

From Figure 7b, we find that well-defined S−O peaks corresponding to the formation of SO_4^{2-} groups (r_{S-O} ∼ 1.5 Å) become progressively stronger in the $Na_{0.5}CoO_2$/Na_3PS_4 interface after 1 ps. We also observe in Figure 7c that clear Co−S peaks (∼ 2.2 Å) correspond to Co_xS_y compounds. Finally, on the basis of the P-containing RDFs (Co−P, Na−P, P−S, P−O, and P−P, given in Figure S5), we may conclude

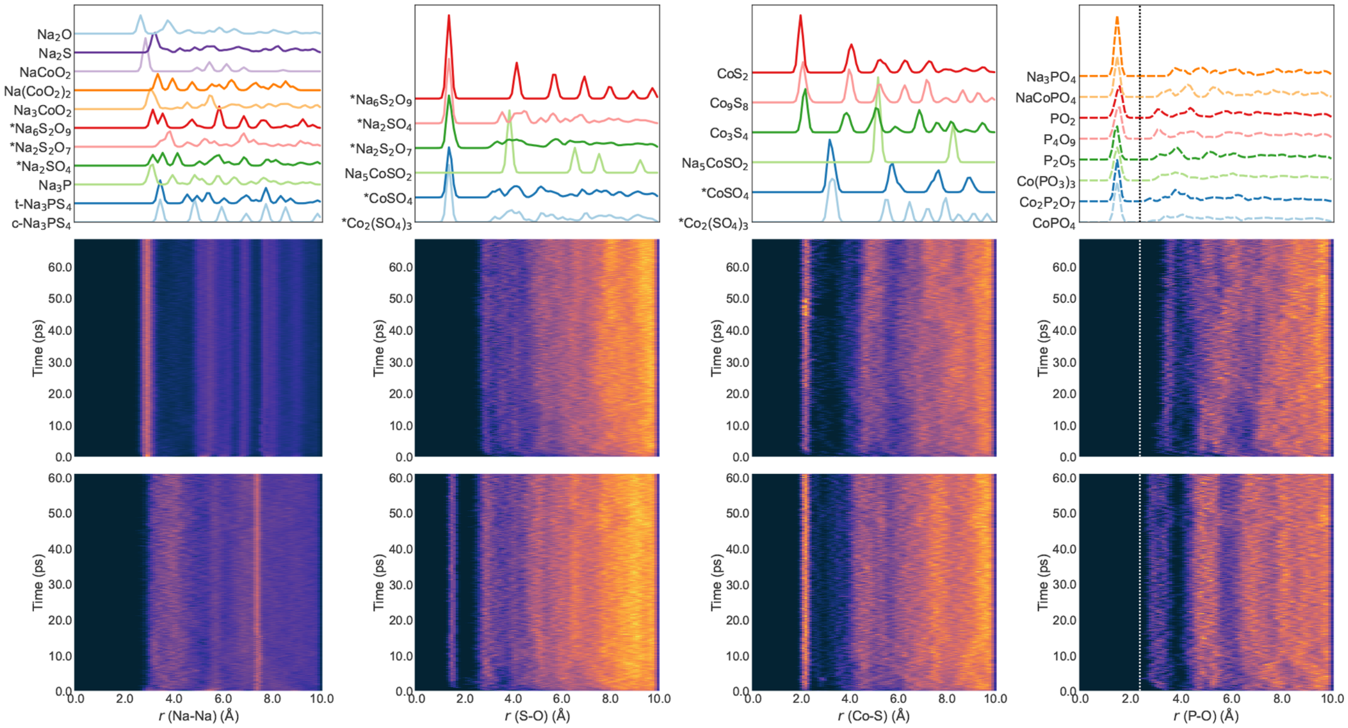

(a) Na-Na pair (b) S-O pair (c) Co-S pair (d) P-O pair

Figure 7. Evolution of the (a) Na–Na, (b) S–O, (c) Co–S, and (d) P–O RDFs of the cathode/SE interfaces with respect to AIMD simulation time. The middle and bottom heat maps are for $NaCoO_2/Na_3PS_4$ and $Na_{0.5}CoO_2/Na_3PS_4$ interfaces, respectively. Note that the references labeled with an asterisk belong to the charged $Na_{0.5}CoO_2/Na_3PS_4$ interface only, and that only some references for the Na–Na and P–O pairs are shown for the sake of clarity.

that Na_3P is the only other phase present at the interface. Indeed, no P–O signatures corresponding to PO_4^{3-} groups [r(P–O) 1.5 Å] are observed (Figure 7d). This result disagrees with the predicted reaction products for the $NaCoO_2/Na_3PS_4$ and CoO_2/Na_3PS_4 interfaces from the thermodynamic approximations, which include Na_3PO_4 and/or $NaCoPO_4$ (see Table S3).

From the findings described above, we may infer that the initial interface reaction favors the formation of SO_4^{2-} and Co_xS_y by the reaction between S from Na_3PS_4 and O and Co from $Na_{0.5}CoO_2$. This is accompanied by the reduction of P in Na_3PS_4 to form Na_3P. We will discuss the possible reasons for the discrepancy between the AIMD results and thermodynamic approximations in the Discussion.

Buffer/Cathode, SE, and Anode Interfaces. From Figure 8 and Figures S7–S9, we find that generally, the Al_2O_3 interfaces with the Na anode, Na_3PS_4 SE, and $NaCoO_2$ cathode are relatively stable, with little change in the RDFs of most bonds. This is consistent with the thermodynamic predictions showing relatively low to zero driving force for the reaction between Al_2O_3 and the electrodes and Na_3PS_4.

■ DISCUSSION

Prediction of Interfacial Reaction Products. Comparing the three approaches to predicting interfacial reactions presented in this work, we may conclude that there is a reasonable agreement between the predicted reaction products and driving forces, especially at the SE/anode interface. To take the Na_3PS_4/Na interface as an example, all approaches predict Na_3P and Na_2S among the interfacial reaction products, in line with experimental findings.[18] The multi-species chemical reactivity (approach 2) and explicit interface modeling (approach 3) approaches predict low reactivities between the commonly used Al_2O_3 buffer material and the cathode, SE, and anode, again in line with experimental findings.[18,21−23]

However, there are significant differences in the predictions of the interfacial reaction products at the more complex cathode/SE interfaces, where multiple species with different mobilities generally participate in the reaction. Here, approach 1 (electrochemical reactivity), in which ultrafast alkali diffusion is assumed, is a rather blunt approximation and predicts the same interfacial products regardless of cathode chemistry.

Approach 2 (chemical reactivity), which assumes a multi-species equilibrium, provides a more realistic picture in the limit of full thermodynamic equilibrium. This limit applies at high temperatures (e.g., synthesis conditions) or long time frames. In general, this approach predicts that mixing of non-polyanion cathodes (e.g., $NaCoO_2$) and polyanion (e.g., PS_4^{3-}) SEs tends to lead to large interfacial reaction energies due to the exchange of the polyanion cation, e.g., to form PO_4^{3-}. This is consistent with previous theoretical and experimental studies.[19]

Finally, approach 3 (kinetic interface model) provides the most realistic picture of interfacial reactivity, albeit at relatively small cell sizes and short time scales. For the $NaCoO_2$ cathode and Na_3PS_4 SE, the AIMD simulations predict that the initial reaction between the two materials, especially in the case of the charged cathode, comprises SO_4^{2-} compounds and Na_3P, with no evidence of PO_4^{3-} formation. We note that the P in Na_3PS_4 is enclosed within PS_4^{3-} tetrahedra. Our hypothesis therefore is that the initial interface reaction takes place via the oxidation

DOI: 10.1021/acs.chemmater.7b04096
Chem. Mater. 2018, 30, 163−173

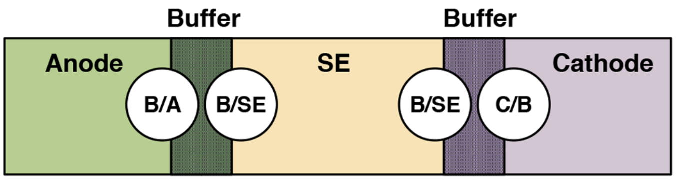

(a) Interfaces in SSNaBs with buffer layer

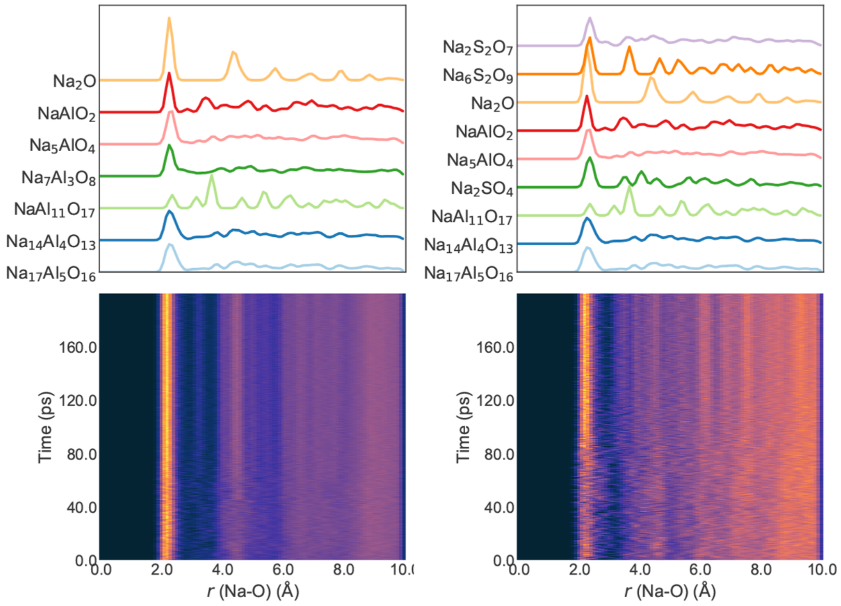

(b) B/A interface (c) B/SE interface

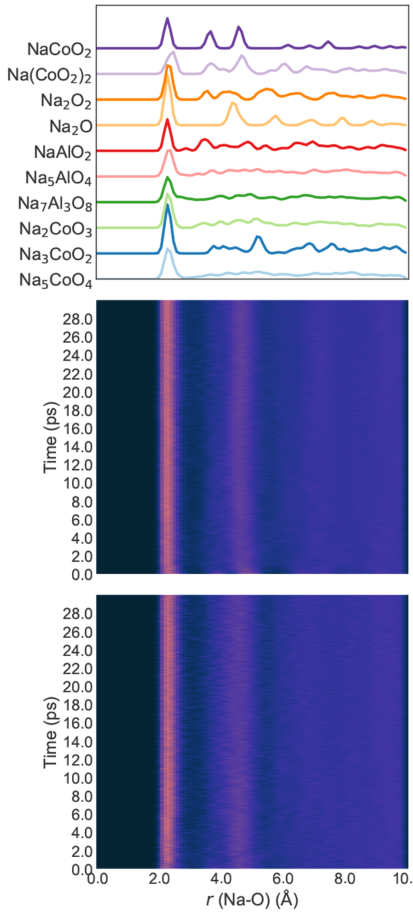

(d) C/B interfaces

Figure 8. (a) Schematic diagram of interfaces in a $NaCoO_2/Na_3PS_4/Na$ SSNaB with an Al_2O_3 buffer layer. Evolution of the Na−O bond in (b) the B/A interface, (c) the B/SE interface, and (d) the C/B interfaces with respect to AIMD simulation time. Note in panel d, the middle and bottom heat maps are for discharged $NaCoO_2/Al_2O_3$ and charged $Na_{0.5}CoO_2/Al_2O_3$ interfaces, respectively, and only some references are shown for the sake of clarity.

of the more accessible S^{2-} on the outside of these tetrahedra by the highly oxidizing cathode to form SO_4^{2-}, with the concomitant reduction of P to form Na_3P. In other words, the formation of the relatively stable SO_4^{2-} groups is kinetically preferred over that of the thermodynamically preferred PO_4^{3-} groups. Once the tightly bound SO_4^{2-} units are formed, we do not observe any further reaction to form PO_4^{3-}. We acknowledge that a possible reason could be that the time scale of our AIMD simulations is too short to observe PO_4^{3-} formation. We have performed additional AIMD simulations of the more reactive charged $Na_{0.5}CoO_2/Na_3PS_4$ interface at an elevated temperature of 600 K; no PO_4^{3-} was observed over 20 ps of simulation time. It should be noted that the voltage in the interface model is not the equilibrium voltage, and hence, the rates of reaction may differ from the true reaction rates in an actual battery cell, especially if long-range electron transfer is involved.[52] Indeed, the predicted phases are relatively consistent across the charged and discharged cathodes, with the main difference being the observed reaction rates. We hope that these predictions can be verified by future experiments, e.g., via XPS characterization of the interface.

It should be noted that all three approaches have limitations, and the best results are obtained by considering the predictions from all three approaches. The chemical and electrochemical activity predictions are computationally relatively inexpensive but make certain simplifying assumptions above the mobilities of the various species. The explicit interface model is more realistic, but its high computational expense limits the length and time scale of the simulations. In addition, the RDF analysis to ascertain the reaction products in the interface simulation becomes combinatorially more complex as the number of species, and hence more candidate RDFs to be analyzed, increases. Nevertheless, we have outlined an elimination approach in which a vast number of candidates can be excluded on the basis of a few bond choices. We believe that this is a useful approach that can be extended to other heterogeneous interfaces beyond energy storage.

Choice of Buffer Layers. Another major finding from our work is the identification of buffer layers for various cathode/SE and anode/SE combinations. Despite the imperfect accuracy in predicting exact reaction products and/or mechanisms (as discussed above), Figure 5 still provides useful guidance about materials selection strategies. We chose to focus on binary oxides in this work because oxides are common and easy to handle, and thin films of binary oxides can be fabricated with well-controlled thicknesses using modern deposition methods such as atomic layer deposition. Most binary oxides are also chemically stable electronic insulators.[51,53]

The main observation from Figure 5 is that buffer layer selection should be tailored according to electrode and SE chemistry. Sc_2O_3, SiO_2, TiO_2, ZrO_2, and HfO_2 all have chemical stability against thiophosphate SEs and TM oxide cathodes that is similar to or even better than that of the commonly used Al_2O_3. On the Na anode/SE interface, the most promising coating materials are Sc_2O_3, ZrO_2, and HfO_2. It should be noted that a key limitation of this analysis is that the diffusion of Na through the buffer layer has not been taken into account. Any buffer material must exhibit reasonable Na diffusivity to ensure that rate capability is not adversely affected, even after accounting for the short diffusion length scales in the buffer layer (typically ∼10−370 nm[17,54] thick).

■ CONCLUSION

To conclude, the reactions at the interfaces among common electrodes, solid electrolytes, and buffer oxides were studied using a range of thermodynamic and kinetic interfacial models in this work. In the limit of full thermodynamic equilibrium, we find that exchange reactions, especially between simple oxides and thiophosphate groups to form PO_4^{3-}, are the main reason for large driving forces for cathode/SE interfacial reactions. Similarly, a high reactivity with large volume changes are predicted at the Na anode/SE interface, while the $Na_2Ti_3O_7$ anode is predicted to be much more stable against a broad range of SEs. We have also identified several promising binary oxide buffer materials with chemical stability with most electrodes and solid electrolytes that is similar to or better than that of the commonly used Al_2O_3. In particular, HfO_2 is a promising candidate that deserves further experimental consideration. Finally, we find that an explicit AIMD simulation of the $NaCoO_2/Na_3PS_4$ interface predicts that the formation of SO_4^{2-}-containing compounds and Na_3P is kinetically favored over the formation of PO_4^{3-}-containing compounds. These insights into interfacial reactions provide useful guidelines for the design of stable electrode/SE and buffer/SE interfaces, a crucial bottleneck in the development of all-solid-state sodium-ion batteries.

■ ASSOCIATED CONTENT

Ⓢ Supporting Information

The Supporting Information is available free of charge on the ACS Publications website at DOI: 10.1021/acs.chemmater.7b04096.

> Selected structures for thermodynamic interfacial reactivity, a plot of Na uptake versus voltage for various SEs, phase equilibria of SEs under different voltage ranges using the grand potential approximation, reaction energies and volume changes of interfacial reactions between selected cathodes in their charged and discharged states and various SEs, products of electrode/SE interfacial reactions using multispecies equilibrium approximation, initial structures of constructed interfaces, and RDF analyses for all constructed interfaces (PDF)

■ AUTHOR INFORMATION

Corresponding Author

*E-mail: ongsp@eng.ucsd.edu.

ORCID

Hanmei Tang: 0000-0003-2659-7768
Zhi Deng: 0000-0002-6311-0608
Zhenbin Wang: 0000-0002-7016-9245
Shyue Ping Ong: 0000-0001-5726-2587

Author Contributions

H.T. and Z.D. contributed equally to this work.

Notes

The authors declare no competing financial interest.

■ ACKNOWLEDGMENTS

This work was supported by the Office of Naval Research (ONR) Young Investigator Program (YIP) under Award N00014-16-1-2621. The authors also acknowledge computational resources provided by the Triton Shared Computing Cluster (TSCC) at the University of California, San Diego, the National Energy Research Scientific Computing Center (NERSC), and the Extreme Science and Engineering Discovery Environment (XSEDE) supported by National Science Foundation Grant ACI-1053575.

■ REFERENCES

(1) Armand, M.; Tarascon, J.-M. Building Better Batteries. *Nature* **2008**, *451*, 652−657.

(2) Takada, K. Progress and Prospective of Solid-State Lithium Batteries. *Acta Mater.* **2013**, *61*, 759−770.

(3) Janek, J.; Zeier, W. G. A Solid Future for Battery Development. *Nat. Energy* **2016**, *1*, 16141.

(4) Goodenough, J.; Hong, H.-P.; Kafalas, J. Fast Na+-Ion Transport in Skeleton Structures. *Mater. Res. Bull.* **1976**, *11*, 203−220.

(5) Inaguma, Y.; Liquan, C.; Itoh, M.; Nakamura, T.; Uchida, T.; Ikuta, H.; Wakihara, M. High Ionic Conductivity in Lithium Lanthanum Titanate. *Solid State Commun.* **1993**, *86*, 689−693.

(6) Murugan, R.; Thangadurai, V.; Weppner, W. Fast Lithium Ion Conduction in Garnet-Type Li7La3Zr2O12. *Angew. Chem., Int. Ed.* **2007**, *46*, 7778−7781.

(7) Kamaya, N.; Homma, K.; Yamakawa, Y.; Hirayama, M.; Kanno, R.; Yonemura, M.; Kamiyama, T.; Kato, Y.; Hama, S.; Kawamoto, K.; Mitsui, A. A Lithium Superionic Conductor. *Nat. Mater.* **2011**, *10*, 682−686.

(8) Seino, Y.; Ota, T.; Takada, K.; Hayashi, A.; Tatsumisago, M. A Sulphide Lithium Super Ion Conductor Is Superior to Liquid Ion Conductors for Use in Rechargeable Batteries. *Energy Environ. Sci.* **2014**, *7*, 627−631.

(9) Hayashi, A.; Noi, K.; Sakuda, A.; Tatsumisago, M. Superionic Glass-Ceramic Electrolytes for Room-Temperature Rechargeable Sodium Batteries. *Nat. Commun.* **2012**, *3*, 856.

(10) Kato, Y.; Hori, S.; Saito, T.; Suzuki, K.; Hirayama, M.; Mitsui, A.; Yonemura, M.; Iba, H.; Kanno, R. High-Power All-Solid-State Batteries Using Sulfide Superionic Conductors. *Nat. Energy* **2016**, *1*, 16030.

(11) Tatsumisago, M.; Hayashi, A. Sulfide Glass-Ceramic Electrolytes for All-Solid-State Lithium and Sodium Batteries. *Int. J. Appl. Glas. Sci.* **2014**, *5*, 226−235.

(12) Hayashi, A.; Noi, K.; Tanibata, N.; Nagao, M.; Tatsumisago, M. High Sodium Ion Conductivity of Glass-Ceramic Electrolytes with Cubic Na3PS4. *J. Power Sources* **2014**, *258*, 420−423.

(13) Banerjee, A.; Park, K. H.; Heo, J. W.; Nam, Y. J.; Moon, C. K.; Oh, S. M.; Hong, S.-T.; Jung, Y. S. Na3SbS4: A Solution Processable Sodium Superionic Conductor for All-Solid-State Sodium-Ion Batteries. *Angew. Chem.* **2016**, *128*, 9786−9790.

(14) Chu, I.-H.; Kompella, C. S.; Nguyen, H.; Zhu, Z.; Hy, S.; Deng, Z.; Meng, Y. S.; Ong, S. P. Room-Temperature All-Solid-State Rechargeable Sodium-Ion Batteries with a Cl-doped Na3PS4 Superionic Conductor. *Sci. Rep.* **2016**, *6*, 33733.

(15) Yu, Z.; Shang, S.-L.; Seo, J.-H.; Wang, D.; Luo, X.; Huang, Q.; Chen, S.; Lu, J.; Li, X.; Liu, Z.-K.; Wang, D. Exceptionally High Ionic Conductivity in Na3P0.62As0.38S4 with Improved Moisture Stability for Solid-State Sodium-Ion Batteries. *Adv. Mater.* **2017**, *29*, 1605561.

(16) Rao, R. P.; Chen, H.; Wong, L. L.; Adams, S. Na3+xMxP1-xS4 (M = Ge 4+, Ti 4+, Sn 4+) Enables High Rate All-Solid-State Na-Ion Batteries Na 2 + 2δ Fe 2-δ (SO4)3 |Na3+xMxP1-xS4 |Na2Ti3O7. *J. Mater. Chem. A* **2017**, *5*, 3377−3388.

(17) Wenzel, S.; Randau, S.; Leichtweiß, T.; Weber, D. A.; Sann, J.; Zeier, W. G.; Janek, J. Direct Observation of the Interfacial Instability of the Fast Ionic Conductor Li10GeP2S12 at the Lithium Metal Anode. *Chem. Mater.* **2016**, *28*, 2400−2407.

(18) Wenzel, S.; Leichtweiss, T.; Weber, D. A.; Sann, J.; Zeier, W. G.; Janek, J. Interfacial Reactivity Benchmarking of the Sodium Ion Conductors Na3PS4 and Sodium *β*-Alumina for Protected Sodium Metal Anodes and Sodium All-Solid-State Batteries. *ACS Appl. Mater. Interfaces* **2016**, *8*, 28216−28224.

(19) Tian, Y.; Shi, T.; Richards, W. D.; Li, J.; Kim, J. C.; Bo, S.; Ceder, G. Compatibility Issues Between Electrodes and Electrolytes in Solid-State Batteries. *Energy Environ. Sci.* **2017**, *10*, 1150−1166.

(20) Han, X.; Gong, Y.; Fu, K. K.; He, X.; Hitz, G. T.; Dai, J.; Pearse, A.; Liu, B.; Wang, H.; Rubloff, G.; Mo, Y.; Thangadurai, V.; Wachsman, E. D.; Hu, L. Negating Interfacial Impedance in Garnet-Based Solid-State Li Metal Batteries. *Nat. Mater.* **2016**, *16*, 572−579.

(21) Ohta, N.; Takada, K.; Zhang, L.; Ma, R.; Osada, M.; Sasaki, T. Enhancement of the High-Rate Capability of Solid-State Lithium Batteries by Nanoscale Interfacial Modification. *Adv. Mater.* **2006**, *18*, 2226−2229.

(22) Ohta, N.; Takada, K.; Sakaguchi, I.; Zhang, L.; Ma, R.; Fukuda, K.; Osada, M.; Sasaki, T. LiNbO3-coated LiCoO2 as Cathode Material for All Solid-State Lithium Secondary Batteries. *Electrochem. Commun.* **2007**, *9*, 1486−1490.

(23) Takada, K.; Ohta, N.; Zhang, L.; Fukuda, K.; Sakaguchi, I.; Ma, R.; Osada, M.; Sasaki, T. Interfacial Modification for High-Power Solid-State Lithium Batteries. *Solid State Ionics* **2008**, *179*, 1333−1337.

(24) Ganesh, P.; Kent, P. R. C.; Jiang, D.-e. Solid Electrolyte Interphase Formation and Electrolyte Reduction at Li-Ion Battery Graphite Anodes: Insights from First-Principles Molecular Dynamics. *J. Phys. Chem. C* **2012**, *116*, 24476−24481.

(25) Ganesh, P.; Jiang, D.-e.; Kent, P. R. C. Accurate Static and Dynamic Properties of Liquid Electrolytes for Li-Ion Batteries from ab initio Molecular Dynamics. *J. Phys. Chem. B* **2011**, *115*, 3085−3090.

(26) Ong, S. P.; Mo, Y.; Richards, W. D.; Miara, L.; Lee, H. S.; Ceder, G. Phase Stability, Electrochemical Stability and Ionic Conductivity of the Li 10 ± 1 MP2 × 12 (M = Ge, Si, Sn, Al or P, and X = O, S or Se) Family of Superionic Conductors. *Energy Environ. Sci.* **2013**, *6*, 148−156.

(27) Mo, Y.; Ong, S. P.; Ceder, G. First Principles Study of the Li10GeP2S12 Lithium Super Ionic Conductor Material. *Chem. Mater.* **2012**, *24*, 15−17.

(28) Zhu, Y.; He, X.; Mo, Y. Origin of Outstanding Stability in the Lithium Solid Electrolyte Materials: Insights from Thermodynamic Analyses Based on First-Principles Calculations. *ACS Appl. Mater. Interfaces* **2015**, *7*, 23685−23693.

(29) Zhu, Y.; He, X.; Mo, Y. First Principles Study on Electrochemical and Chemical Stability of Solid Electrolyte-Electrode Interfaces in All-Solid-State Li-Ion Batteries. *J. Mater. Chem. A* **2016**, *4*, 3253−3266.

(30) Richards, W. D.; Miara, L. J.; Wang, Y.; Kim, J. C.; Ceder, G. Interface Stability in Solid-State Batteries. *Chem. Mater.* **2016**, *28*, 266−273.

(31) Miara, L. J.; Richards, W. D.; Wang, Y. E.; Ceder, G. First-Principles Studies on Cation Dopants and Electrolyte|Cathode Interphases for Lithium Garnets. *Chem. Mater.* **2015**, *27*, 4040−4047.

(32) Chu, I.-H.; Nguyen, H.; Hy, S.; Lin, Y.-C.; Wang, Z.; Xu, Z.; Deng, Z.; Meng, Y. S.; Ong, S. P. Insights into the Performance Limits of the Li7P3S11 Superionic Conductor: A Combined First-Principles and Experimental Study. *ACS Appl. Mater. Interfaces* **2016**, *8*, 7843−7853.

(33) Ping Ong, S.; Wang, L.; Kang, B.; Ceder, G. Li-Fe-P-O2 Phase Diagram from First Principles Calculations. *Chem. Mater.* **2008**, *20*, 1798−1807.

(34) Kramer, D.; Ceder, G. Tailoring the Morphology of LiCoO2: A First Principles Study. *Chem. Mater.* **2009**, *21*, 3799−3809.

(35) Haruyama, J.; Sodeyama, K.; Han, L.; Takada, K.; Tateyama, Y. Space-Charge Layer Effect at Interface between Oxide Cathode and Sulfide Electrolyte in All-Solid-State Lithium-Ion Battery. *Chem. Mater.* **2014**, *26*, 4248−4255.

(36) Stradi, D.; Jelver, L.; Smidstrup, S.; Stokbro, K. Method for Determining Optimal Supercell Representation of Interfaces. *J. Phys.: Condens. Matter* **2017**, *29*, 185901.

(37) Jain, A.; Ong, S. P.; Hautier, G.; Chen, W.; Richards, W. D.; Dacek, S.; Cholia, S.; Gunter, D.; Skinner, D.; Ceder, G.; Persson, K. A. Commentary: The Materials Project: A Materials Genome Approach to Accelerating Materials Innovation. *APL Mater.* **2013**, *1*, 011002.

(38) Ong, S. P.; Cholia, S.; Jain, A.; Brafman, M.; Gunter, D.; Ceder, G.; Persson, K. a. The Materials Application Programming Interface (API): A Simple, Flexible and Efficient API for Materials Data Based on Representational State Transfer (REST) Principles. *Comput. Mater. Sci.* **2015**, *97*, 209−215.

(39) Kresse, G.; Furthmüller, J. Efficient Iterative Schemes for Ab Initio Total-Energy Calculations Using a Plane-Wave Basis Set. *Phys. Rev. B: Condens. Matter Mater. Phys.* **1996**, *54*, 11169−11186.

(40) Blöchl, P. E. Projector Augmented-Wave Method. *Phys. Rev. B: Condens. Matter Mater. Phys.* **1994**, *50*, 17953−17979.

(41) Perdew, J. P.; Burke, K.; Ernzerhof, M. Generalized Gradient Approximation Made Simple. *Phys. Rev. Lett.* **1996**, *77*, 3865−3868.

(42) Jain, A.; Hautier, G.; Ong, S. P.; Moore, C. J.; Fischer, C. C.; Persson, K. A.; Ceder, G. Formation Enthalpies by Mixing GGA and GGA + U Calculations. *Phys. Rev. B: Condens. Matter Mater. Phys.* **2011**, *84*, 045115.

(43) Ong, S. P.; Richards, W. D.; Jain, A.; Hautier, G.; Kocher, M.; Cholia, S.; Gunter, D.; Chevrier, V. L.; Persson, K. a.; Ceder, G. Python Materials Genomics (Pymatgen): A Robust, Open-Source Python Library for Materials Analysis. *Comput. Mater. Sci.* **2013**, *68*, 314−319.

(44) Parrinello, M.; Rahman, A. Crystal Structure and Pair Potentials: A Molecular-Dynamics Study. *Phys. Rev. Lett.* **1980**, *45*, 1196−1199.

(45) Deng, Z.; Zhu, Z.; Chu, I.-H.; Ong, S. P. Data-Driven First-Principles Methods for the Study and Design of Alkali Superionic Conductors. *Chem. Mater.* **2017**, *29*, 281−288.

(46) Zhang, L.; Zhang, D.; Yang, K.; Yan, X.; Wang, L.; Mi, J.; Xu, B.; Li, Y. Vacancy-Contained Tetragonal Na3SbS4 Superionic Conductor. *Adv. Sci.* **2016**, *3*, 1600089.

(47) Chen, Z.; Qin, Y.; Amine, K.; Sun, Y.-K. Role of Surface Coating on Cathode Materials for Lithium-Ion Batteries. *J. Mater. Chem.* **2010**, *20*, 7606−7612.

(48) He, Y.; Yu, X.; Wang, Y.; Li, H.; Huang, X. Alumina-Coated Patterned Amorphous Silicon as the Anode for a Lithium-Ion Battery with High Coulombic Efficiency. *Adv. Mater.* **2011**, *23*, 4938−4941.

(49) Cho, J.; Kim, Y. J.; Park, B. Novel $LiCoO_2$ Cathode Material with Al_2O_3 Coating for a Li Ion Cell. *Chem. Mater.* **2000**, *12*, 3788−3791.

(50) Yesibolati, N.; Shahid, M.; Chen, W.; Hedhili, M. N.; Reuter, M. C.; Ross, F. M.; Alshareef, H. N. SnO2 Anode Surface Passivation by Atomic Layer Deposited HfO2 Improves Li-Ion Battery Performance. *Small* **2014**, *10*, 2849−2858.

(51) Ahmed, B.; Anjum, D. H.; Hedhili, M. N.; Alshareef, H. N. Mechanistic Insight into the Stability of HfO2 -Coated MoS2 Nanosheet Anodes for Sodium Ion Batteries. *Small* **2015**, *11*, 4341−4350.

(52) Leung, K. Predicting the Voltage Dependence of Interfacial Electrochemical Processes at Lithium-Intercalated Graphite Edge Planes. *Phys. Chem. Chem. Phys.* **2015**, *17*, 1637−1643.

(53) Sumita, M.; Tanaka, Y.; Ikeda, M.; Ohno, T. Charged and Discharged States of Cathode/Sulfide Electrolyte Interfaces in All-Solid-State Lithium Ion Batteries. *J. Phys. Chem. C* **2016**, *120*, 13332−13339.

(54) Sakuda, A.; Hayashi, A.; Tatsumisago, M. Interfacial Observation between LiCoO2 Electrode and Li2S-P2S5 Solid Electrolytes of All-Solid-State Lithium Secondary Batteries Using Transmission Electron Microscopy. *Chem. Mater.* **2010**, *22*, 949−956.

(55) Hong, H. Y. P. Crystal Structures and Crystal Chemistry in the System Na1+xZr2SixP3-xO12. *Mater. Res. Bull.* **1976**, *11*, 173−182.

(56) Wang, H.; Chen, Y.; Hood, Z. D.; Sahu, G.; Pandian, A. S.; Keum, J. K.; An, K.; Liang, C. An Air-Stable Na3SbS4 Superionic Conductor Prepared by a Rapid and Economic Synthetic Procedure. *Angew. Chem., Int. Ed.* **2016**, *55*, 8551−8555.

(57) Zhang, L.; Yang, K.; Mi, J.; Lu, L.; Zhao, L.; Wang, L.; Li, Y.; Zeng, H. Na3PSe4: A Novel Chalcogenide Solid Electrolyte with High Ionic Conductivity. *Adv. Energy Mater.* **2015**, *5*, 1501294.

(58) Bo, S.-H.; Wang, Y.; Kim, J. C.; Richards, W. D.; Ceder, G. Computational and Experimental Investigations of Na-Ion Conduction in Cubic Na 3 PSe 4. *Chem. Mater.* **2016**, *28*, 252−258.

(59) Komaba, S.; Takei, C.; Nakayama, T.; Ogata, A.; Yabuuchi, N. Electrochemical Intercalation Activity of Layered NaCrO2 vs. LiCrO2. *Electrochem. Commun.* **2010**, *12*, 355−358.

(60) Vassilaras, P.; Ma, X.; Li, X.; Ceder, G. Electrochemical Properties of Monoclinic NaNiO2. *J. Electrochem. Soc.* **2013**, *160*, A207−A211.

(61) Yabuuchi, N.; Yoshida, H.; Komaba, S. Crystal Structures and Electrode Performance of Alpha-NaFeO2 for Rechargeable Sodium Batteries. *Electrochemistry* **2012**, *80*, 716−719.

(62) Ge, P.; Fouletier, M. Electrochemical Intercalation of Sodium in Graphite. *Solid State Ionics* **1988**, *28−30*, 1172−1175.

(63) Whittingham, M. Chemistry of Intercalation Compounds: Metal Guests in Chalcogenide Hosts. *Prog. Solid State Chem.* **1978**, *12*, 41−99.

(64) Oh, S.-M.; Myung, S.-T.; Hassoun, J.; Scrosati, B.; Sun, Y.-K. Reversible NaFePO4 Electrode for Sodium Secondary Batteries. *Electrochem. Commun.* **2012**, *22*, 149−152.

(65) Kawabe, Y.; Yabuuchi, N.; Kajiyama, M.; Fukuhara, N.; Inamasu, T.; Okuyama, R.; Nakai, I.; Komaba, S. Synthesis and Electrode Performance of Carbon Coated Na2FePO4F for Rechargeable Na Batteries. *Electrochem. Commun.* **2011**, *13*, 1225−1228.

(66) Jian, Z.; Zhao, L.; Pan, H.; Hu, Y.-S.; Li, H.; Chen, W.; Chen, L. Carbon Coated Na3V2(PO4)3 as Novel Electrode Material for Sodium Ion Batteries. *Electrochem. Commun.* **2012**, *14*, 86−89.

(67) Shakoor, R. a.; Seo, D.-H.; Kim, H.; Park, Y.-U.; Kim, J.; Kim, S.-W.; Gwon, H.; Lee, S.; Kang, K. A Combined First Principles and Experimental Study on Na3V2(PO4)2F3 for Rechargeable Na Batteries. *J. Mater. Chem.* **2012**, *22*, 20535.

(68) Barpanda, P.; Oyama, G.; Nishimura, S.-i.; Chung, S.-C.; Yamada, A. A 3.8-V Earth-Abundant Sodium Battery Electrode. *Nat. Commun.* **2014**, *5*, 4358.

(69) Senguttuvan, P.; Rousse, G.; Seznec, V.; Tarascon, J.-M.; Palacín, M. Na2Ti3O7: Lowest Voltage Ever Reported Oxide Insertion Electrode for Sodium Ion Batteries. *Chem. Mater.* **2011**, *23*, 4109−4111.

DOI: 10.1021/acs.chemmater.7b04096
Chem. Mater. 2018, 30, 163−173